

Brittany Northcutt

Issam Mudawar¹

e-mail: mudawar@ecn.purdue.edu

Boiling and Two-Phase Flow Laboratory
(BTPFL),
Purdue University International Electronic
Cooling Alliance (PUIECA),
Mechanical Engineering Building,
585 Purdue Mall,
West Lafayette, IN 47907;
Rolls-Royce Purdue University Technology
Center (UTC),
Maurice Zucrow Laboratories,
500 Allison Road,
Purdue University,
West Lafayette, IN 47907

Enhanced Design of Cross-Flow Microchannel Heat Exchanger Module for High-Performance Aircraft Gas Turbine Engines

This study explores the design of highly compact air–fuel heat exchangers for high-performance aircraft turbine engines. The heat exchangers consist of a large number of modules that can be brazed together into a rectangular or annular outer envelope. Inside the module, fuel flows through parallel microchannels, while air flows externally perpendicular to the direction of the fuel flow over rows of short, straight fins. A theoretical model recently developed by the authors for a single module is both validated experimentally, by simulating aircraft fuel with water, and expanded to actual heat exchangers and JP-8 aircraft fuel. An optimization study of the module's geometrical parameters is conducted for high-pressure-ratio engine conditions in pursuit of the highest heat transfer rate. These parameters are then adjusted based on such considerations as microfabrication limits, stress and rupture, and the need to preclude clogging of the fuel and air passage. Using the revised parameters, the analytical model is used to generate effectiveness plots for both rectangular and annular heat exchangers with one air pass and one, two, or three fuel passes. These results demonstrate both the effectiveness of the module design and the versatility of the analytical tools at designing complex heat exchangers for high-performance aircraft gas turbine engines. [DOI: 10.1115/1.4006037]

Keywords: microchannel, cross-flow heat exchanger, gas turbine engines

1 Introduction

One effective means to enhancing the performance of aircraft gas turbine engines is to increase the compressor pressure ratio. However, high-pressure ratios increase the temperature of air exiting the compressor, which is often the primary coolant for downstream engine components such as turbine blades and afterburner walls. While compressor bleed air can adequately cool turbine blades in conventional engines [1], the bleed air temperature is far too high in high-pressure-ratio engines. This necessitates the use of a heat exchanger to precool the bleed air before it is supplied to the downstream engine components.

Two possible heat sinks are available for the compressor bleed air in a high-pressure-ratio engine, the engine fan's bypass air, and the fuel [2,3]. While there are advantages and disadvantages to using each, the higher heat capacity of the fuel can result in a more compact and lightweight heat exchanger [2], which is the basis for selecting the fuel as heat sink for the present study.

The quest for better turbine engine performance has spurred several efforts to develop innovative air–fuel heat exchangers. Most of these efforts were focused on techniques to enhance heat transfer performance on the air or the fuel sides of the heat exchanger separately using predominantly air cross-flow over circular fuel-carrying tubes [3–5].

Recent high-performance heat exchanger developments in applications other than those intended for gas turbine engines provide valuable lessons concerning fuel side heat transfer enhancement. Most promising among these developments is the use of micro/minichannels [6,7], jets [8,9], and sprays [10], and surface augmentation techniques [11]. Use of micro/minichannels is espe-

cially attractive to the present application given the stringent volume and weight constraints of gas turbine engines.

Recently, Nacke et al. [12] proposed a radically different air–fuel heat exchanger design for high-pressure-ratio turbine engines. Unlike the tube cross-flow design predecessors, their heat exchanger consisted of a large number of compact, cross-flow microchannel modules, whose design is depicted in Fig. 1(a). Within each module, the fuel flows through a series of parallel microchannels, a design similar to that adopted for cooling high-heat-flux electronic chips, lasers, and radar devices [7]. The air flows over rows of short, straight fins, arranged so that the air flow is perpendicular to the fuel flow. Using short fins instead of continuous, longer fins increase the airside heat transfer performance by taking advantage of the thin reinitiated boundary layers [6]. A key advantage of this design is that modules can be arranged in a variety of heat exchanger design envelopes based on the constraints of the particular turbine engine. Two such designs are the rectangular heat exchanger, Fig. 1(b), and annular heat exchanger, Fig. 1(c). In the rectangular design, several modules are stacked together to form a single heat exchanger pass, with several passes forming the full heat exchanger. Figure 1(b) shows the air flowing straight through all the passes, while the fuel flows in alternating directions between consecutive passes. In the annular design, modules of each pass are arranged in a cylinder, with the full heat exchanger consisting of concentric cylinders of passes. The airside fins are angled to allow for closer packing of modules in each pass. Figure 1(c) shows that the air flowing radially inward through the heat exchanger passes and exiting axially along the axis, while the fuel, like in the rectangular design, reverses direction between passes.

The primary goals of the earlier study by Nacke et al. [12] were to (1) present a theoretical model for predicting the mean outlet temperatures of the air and fuel for a single module and (2) experimentally validate the predicted performance by testing a single module using water to simulate aircraft fuel. The present study aims to extend the Nacke et al. study to full rectangular and

¹Corresponding author.

Contributed by the Heat Transfer Division of ASME for publication in the JOURNAL OF HEAT TRANSFER. Manuscript received May 18, 2011; final manuscript received November 28, 2011; published online May 8, 2012. Assoc. Editor: Phillip M. Ligrani.

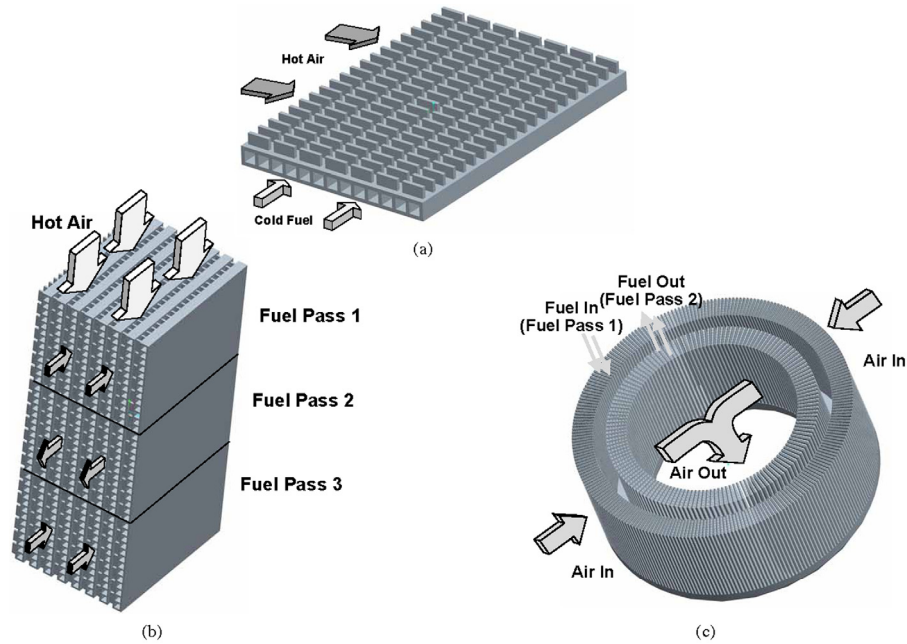


Fig. 1 (a) Cross-flow microchannel air–fuel heat exchanger module, (b) rectangular heat exchanger configuration (shown with one air pass and three fuel passes), and (c) annular heat exchanger configuration (shown with one air pass and two fuel passes)

annular heat exchangers. First, issues concerning practical stacking of many modules in an actual heat exchanger and the impact of stacking on thermal boundary conditions between modules are discussed. Second, a new thermal design methodology is presented and its predictions validated against single module air–water data. Third, the module design parameters are discussed both in terms of practical engine requirements and ranges that may be considered in optimizing the thermal performance of the module for JP-8 jet fuel. Finally, effectiveness predictions are presented for both rectangular and annular heat exchangers under high-pressure-ratio conditions.

2 Experimental Methods

2.1 Test Facility. The test facility used in this study was described in detail in Ref. [12]. This facility uses air and water supply lines to simulate, respectively, the air and the fuel flows through a heat exchanger in a high-performance turbine engine. The heat exchanger test module is held in place by a polyether ether ketone (PEEK) plastic housing, which also provides thermal insulation for the flows.

2.2 Test Module. The heat exchanger test module is fabricated from stainless steel and measures 76.2 mm long and 15.24 mm wide, with two 5.08 mm extended end regions used to press fit the module into the PEEK housing. Since the end regions do not contribute to heat transfer between the air and the liquid, the working length of the module is 66.04 mm.

Figure 2 shows that the airside of the module consists of 65 rows of fins, with each row containing seven fins. Six of the fins are 1.524 mm long, while the middle fin is 2.032 mm long. The fin tops are sloped, with the fin height varying from 0.127 mm to 0.635 mm, forming a 2.29 deg angle with the test module surface. This tapered design would enable modules to be stacked in the annular heat exchanger configuration depicted in Fig. 1(c). The waterside of the module consists of 26 rectangular microchannels that run the entire length of the module. These microchannels are 0.254 mm wide by 0.762 mm high. Figure 2(c) shows actual photos of the test module.

2.3 Measurement Accuracy. Temperatures throughout the facility are measured by type-K thermocouples with an accuracy of $\pm 0.5^\circ\text{C}$. Pressures are measured using Druck absolute and differential transducers with accuracies of $\pm 0.04\%$ and $\pm 0.25\%$, respectively, of full-scale reading. The air speed is measured by one of two sonic venturi flow meters manufactured to ASME standards with a reading accuracy of $\pm 1\%$. The waterside flow rates are measured by three flow meters that have accuracies of $\pm 6\%$, $\pm 3\%$, and $\pm 3\%$, over flow rate ranges of 0–441, 0–3784, and 0–18,930 cm^3/min , respectively.

3 Heat Exchanger Model

3.1 Overall Heat Exchanger Modeling Approach. Methods for determining the heat transfer effectiveness for different types of heat exchangers, such as the number of transfer units (NTU) method and the log mean temperature difference method (LMTD), are readily available from the heat transfer literature [13]. These methods provide means for determining global heat exchanger parameters without the need to explore the detailed temperature variations within the heat exchanger. While the heat exchanger examined in the present study is a cross-flow heat exchanger, for which both the NTU and LMTD methods provide generalized solutions, the authors opted to avoid relying on these methods for two reasons: (1) concerns over the applicability of generalized heat exchanger models, which are well validated for conventional heat exchanger, to a cross-flow heat exchanger with small (micro) flow features on both the liquid and the airside, and (2) importance of determining *local* temperature variations in the two fluids as well as the metal wall to gas turbine air–fuel heat exchangers. The second reason is based on the need to evaluate the effects of local temperatures on potential chemical de-composition of the fuel as well as partial change of phase of fuel from liquid to vapor; both can have substantive influences on the performance of the heat exchanger for this application.

These limitations of the generalized heat exchanger methods created a preference to implementing detailed solutions for differential equations governing cross-flow heat exchangers. This

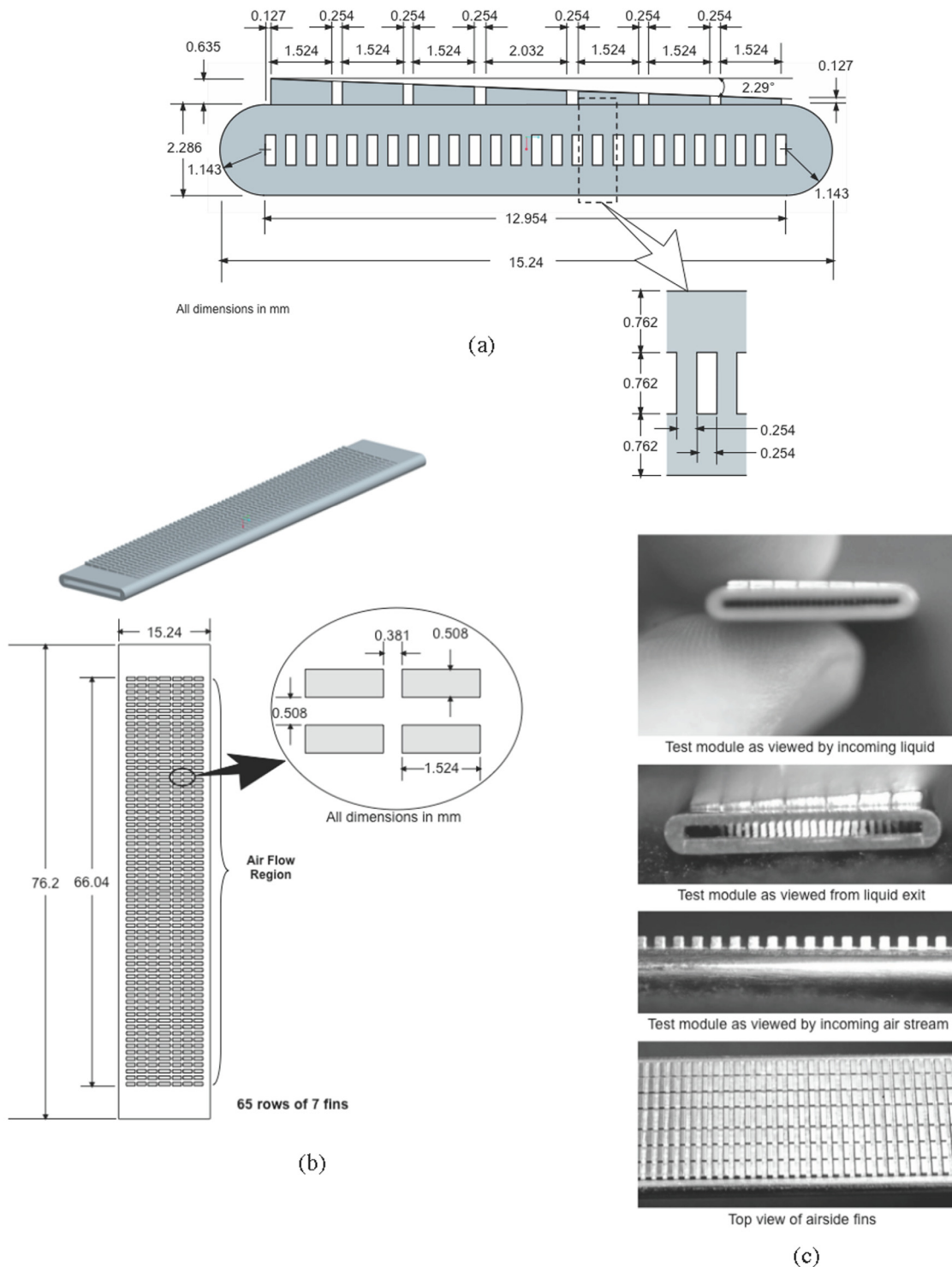


Fig. 2 Test module: (a) side view depicting fuel microchannel dimensions and profiles of airside fins and (b) top view depicting rows of airside fins. (c) Various photos of test module

method is used to determine the temperature distributions for both the air and the fuel streams for a single module. Separately, a method is presented to determine the mean overall heat transfer coefficient, U , between the air and the fuel sides.

The model adopted in this study is used to determine temperatures of the hot air stream, $T_h = T_h(x, y)$, and cold fluid stream, $T_c = T_c(x, y)$, as illustrated in Fig. 3(a). Using a model presented by Mason [14] and integral relations from Ref. [15], Nacke et al. [12] showed that the total heat transfer rate for the entire module can be calculated according to

$$\phi = \frac{q}{UWL [T_h(0, 0) - T_c(0, 0)]} = \frac{1}{ab} \sum_{n=0}^{\infty} \left[1 - e^{-a} \sum_{k=0}^n \frac{a^k}{k!} \right] \left[1 - e^{-b} \sum_{k=0}^n \frac{b^k}{k!} \right] \quad (1)$$

where

$$a = \frac{UWL}{\dot{m}_h C_{p,h}} \quad (2a)$$

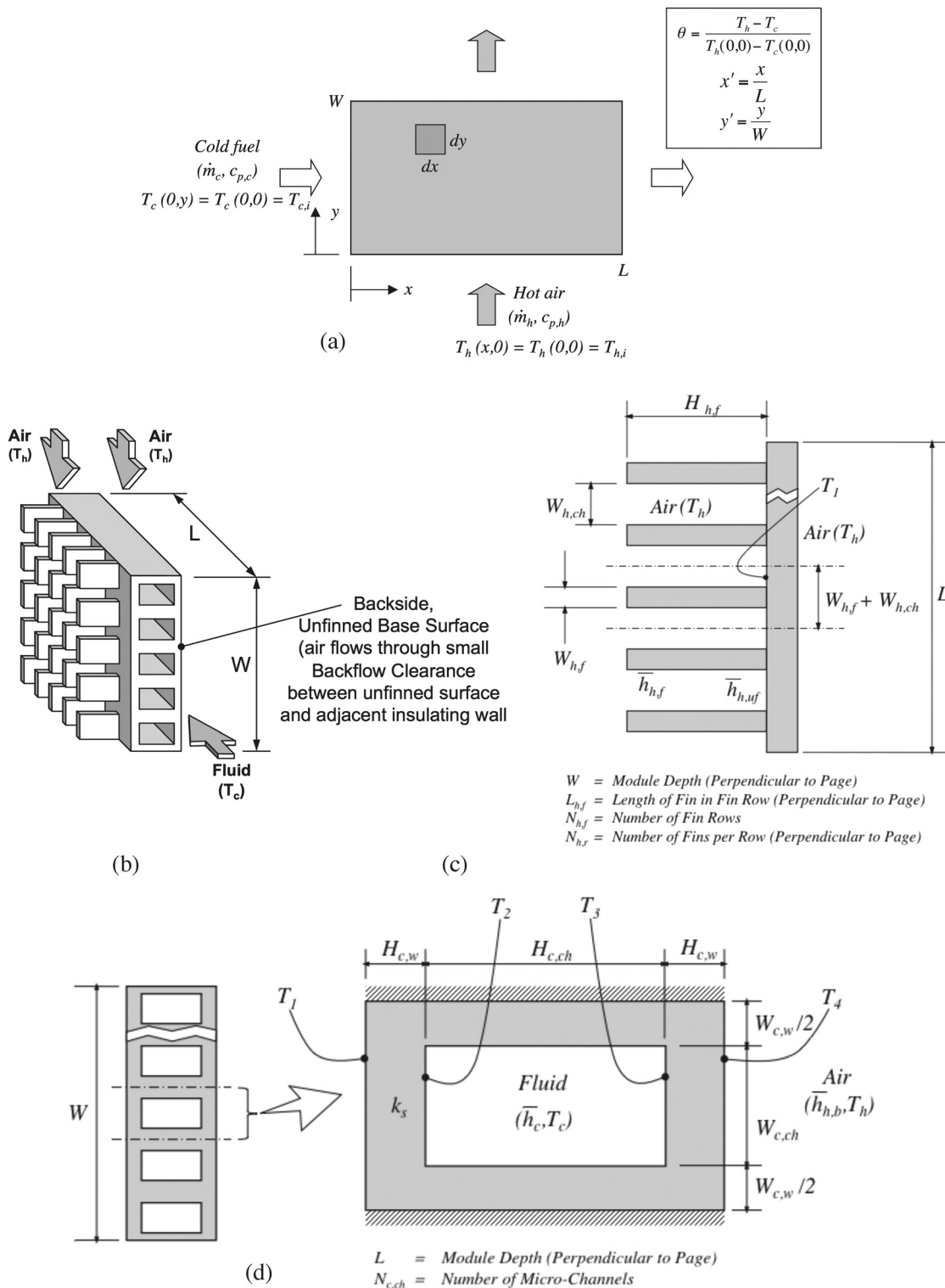


Fig. 3 Schematics and nomenclature of: (a) overall model for cross-flow microchannel heat exchanger module with uniform inlet fluid temperatures, (b) test module, (c) finned airside boundary, and (d) fuel microchannels and unfinned airside boundaries

and

$$b = \frac{UWL}{\dot{m}_c c_{p,c}} \quad (2b)$$

Details concerning the determination of the heat exchanger's mean hot stream outlet temperature, $\bar{T}_{h,o}$, and mean cold stream outlet temperature, $\bar{T}_{c,o}$, are provided in Ref. [12].

3.2 Overall Heat Transfer Coefficient. The overall heat transfer coefficient, U , in Eq. (1) can be determined via a thermal resistance network representing the heat exchanger module geometry illustrated in Fig. 3(b). Air flows along both the finned and the back sides of the module, while the liquid flows through the internal microchannels. Details of the airside and fluid-side boundaries are given in Figs. 3(c) and 4(d). The numbers of airside fin rows, $N_{h,f}$,

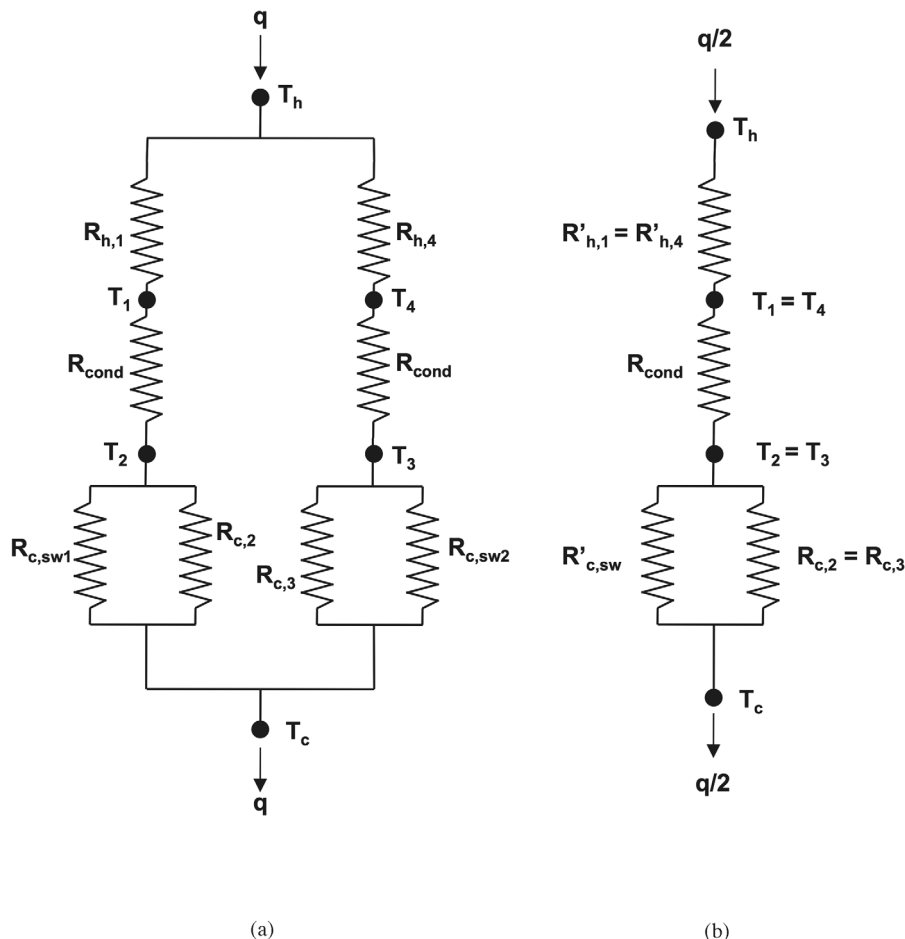


Fig. 4 Equivalent thermal resistance network representing: (a) entire microchannel test module and (b) symmetrical module design used in actual heat transfer analysis

and fuel-side microchannels, $N_{c,ch}$, are given by $N_{h,f} = L/(W_{h,ch} + W_{h,f})$ and $N_{c,ch} = W/(W_{c,ch} + W_{c,w})$, respectively.

The finned airside (surface 1) heat transfer rate, $q_{h,1}$, is a function of the airside fin efficiency, $\eta_{h,f}$, and average airside heat transfer coefficients for the finned and base surfaces, $\bar{h}_{h,f}$ and $\bar{h}_{h,uf}$, respectively; relations for these parameters are available from Ref. [13].

As shown in Ref. [12], the heat transfer rate from surface 1 can be expressed in terms of an airside resistance, $R_{h,1}$, for surface 1 by the relation

$$q_{h,1} = \frac{T_h - T_1}{\left\{ \frac{1}{N_{h,f} [\eta_{h,f} \bar{h}_{h,f} A_{h,f} + \bar{h}_{h,uf} A_{h,uf}]} \right\}} = \frac{T_h - T_1}{R_{h,1}} \quad (3)$$

Assuming the inner surface temperature for the outer wall, T_2 , is uniform, and one-dimensional conduction across the outer wall, the airside heat transfer rate can be represented in terms of an outer wall conduction resistance, R_{cond} , by

$$q''_s (LW) = \frac{T_1 - T_2}{\left\{ \frac{H_{c,w}}{k_s (LW)} \right\}} = \frac{T_1 - T_2}{R_{cond}} \quad (4)$$

By approximating the microchannel sidewalls as fins with prescribed tip temperature (see Ref. [13]), the rate of heat flow through the sidewalls can be broken into the difference between two separate heat flow terms. This procedure is used to derive expressions for fluid-sidewall resistances $R_{c,sw1}$ and $R_{c,sw2}$.

$$q_{c,sw} = \frac{T_2 - T_c}{\left\{ \frac{1}{N_{c,ch} \sqrt{\bar{h}_c P_{c,f} k_s A_{c,csf} \coth \left(\sqrt{\frac{\bar{h}_c P_{c,f}}{k_s A_{c,csf}}} H_{c,ch} \right)}} \right\}} - \frac{T_3 - T_c}{\left\{ \frac{1}{N_{c,ch} \sqrt{\bar{h}_c P_{c,f} k_s A_{c,csf} \csc h \left(\sqrt{\frac{\bar{h}_c P_{c,f}}{k_s A_{c,csf}}} H_{c,ch} \right)}} \right\}} = \frac{T_2 - T_c}{R_{c,sw1}} - \frac{T_3 - T_c}{R_{c,sw2}} \quad (5)$$

There is also direct convective heat transfer from surface 2 of the microchannel to the liquid, which is given by

$$q_{c,2} = \frac{(T_2 - T_c)}{\left\{ \frac{1}{N_{c,ch} \bar{h}_c (W_{c,ch} L)} \right\}} = \frac{(T_2 - T_c)}{R_{c,2}} \quad (6)$$

The heat transfer rate between surface 3 and the liquid is given by

$$q_{c,3} = \frac{(T_3 - T_c)}{\left\{ \frac{1}{N_{c,ch} \bar{h}_c (W_{c,ch} L)} \right\}} = \frac{(T_3 - T_c)}{R_{c,3}} \quad (7)$$

Heat transfer from the unfinned airside is associated with a conduction resistance similar to that given by Eq. (4).

On the backside of the heat exchanger module, heat is transferred by convection according to

$$q_{a,b} = \frac{(T_h - T_4)}{\left\{ \frac{1}{h_{h,b}(WL)} \right\}} = \frac{(T_h - T_4)}{R_{h,4}} \quad (8)$$

The overall heat transfer coefficient, U , can be determined from the module's total thermal resistance, R_{tot} , according to the relation

$$U = \frac{1}{(WL) R_{tot}} \quad (9)$$

Figure 4(a) shows that the total resistance may be represented as the equivalent of two parallel branches A and B , with each consisting of a series of three resistances; the third of which is the equivalent of two parallel resistances

$$R_{tot} = \frac{R_A R_B}{R_A + R_B} \quad (10a)$$

where

$$R_A = R_{h,1} + R_{cond} + \frac{R_{c,sw1} R_{c,2}}{R_{c,sw1} + R_{c,2}} \quad (10b)$$

and

$$R_B = R_{h,4} + R_{cond} + \frac{R_{c,cw2} R_{c,3}}{R_{c,cw2} + R_{c,3}} \quad (10c)$$

3.3 Determination of Airside and Fluid-Side Heat Transfer Coefficients and Fin Efficiencies. Calculating the overall heat transfer coefficient requires determination of the airside and fluid-side heat transfer coefficients as well as fin efficiencies. To accomplish this task, the module geometry, air and fluid inlet conditions, and air and fluid properties must be initialized. In the present study, water was used to simulate the fuel stream. The air and water properties were determined using EES [16].

In the airside fin calculations, laminar flow over a flat plate is assumed, based on the low Reynolds numbers associated with the present application and the experimental validation study. For this assumption to be valid for the entire air passage between two adjacent rows of fins, the boundary layer thickness must be smaller than the spacing between fin rows. Otherwise, the boundary layers

would merge, and the air flow would resemble internal instead of external flow. The airside fin efficiency can be determined by using the approximation for a fin with an adiabatic tip because $\bar{h}_{h,f} W_{h,f} / k_s \leq 0.0625$ for the present study. Laminar flow over a flat plate is also assumed for the airside base calculations between fins. As with the airside fins, this assumption is valid if the boundary layers for the base and the adjacent module (or PEEK housing in the experimental study) do not merge, which would change the flow from external to internal.

Unlike the finned side, the air flow along the back of the module (surface 4 in Fig. 3(d)) is internal, given the small back flow clearance s_2 . Here, a correlation for laminar flow in a channel with an equivalent hydraulic diameter is used.

The fuel-side convection coefficient is determined from correlations for flow in a circular channel that is corrected for equivalent hydraulic diameter of the microchannel. Three different correlations are recommended based on Prandtl number and Reynolds number ranges. These correlations differ slightly from those used by Nacke et al. Table 1 provides all correlations or relations for the airside and fluid-side heat transfer coefficients and fins [13,17,18] that are used to evaluate the overall heat transfer coefficient U .

3.4 Expansion of Model for Use in Actual Heat Exchangers. Adapting the analytical model developed thus far for the single experimental heat exchanger module to an actual heat exchanger involves fundamental changes to the module's thermal boundary conditions that will have profound influences on values of some of the resistances in the network shown in Fig. 4(a). The previous analysis involved a single module that is mounted inside a thermally insulating housing, while the analysis for a module in an actual heat exchanger must take into account the actual construction of the heat exchanger, where the airside fins of each module are brazed directly to the adjacent module. With such a configuration, the module will interact thermally with adjacent modules.

Figure 5 shows the fundamental differences between the thermal boundary conditions in the experimental setup, Fig. 5(a), compared to those encountered in a rectangular heat exchanger, Fig. 5(b), or an annular heat exchanger, Fig. 5(c). Assuming no contact resistance is present along the brazing interfaces between adjacent modules in the actual heat exchangers, symmetry is achieved both in geometry and boundary conditions when considering a cell that includes on both sides air fins half the height of that considered in the experimental setup. Because of symmetry, the airside fins are adiabatic halfway along their height.

Table 1 Heat transfer coefficient and fin efficiency equations

Module section	Equation
Air flow on finned side of module along fins	Heat transfer coefficient: $\bar{Nu}_{h,f} = \frac{\bar{h}_{h,f} L_{h,f}}{k_n} = 0.664 Re_{h,f}^{1/2} Pr_h^{1/3}$ where $Re_{h,f} = \frac{V_h L_{h,f}}{\nu_h}$, valid for $\delta_{h,f} < W_{h,cf}/2$ Fin efficiency: Experimental module: $\eta_{h,f} = \frac{\tanh(m_h H_{h,fe})}{m_h H_{h,fe}}$, $H_{h,fe} = H_{h,f} + W_{h,f}/2$ Actual heat exchanger: $\eta'_{h,f} = \frac{\tanh\left(\frac{m_h H_{h,f}}{2}\right)}{m_h \left(\frac{H_{h,f}}{2}\right)}$ where $m_h = \sqrt{\frac{\bar{h}_{h,f} P_{h,f}}{k_s A_{h,csf}}}$, $P_{h,f} = 2(W_{h,f} + L_{h,f})$, $A_{h,csf} = W_{h,f} L_{h,f}$
Air flow on finned side of module between fins	Heat transfer coefficient: $\bar{Nu}_{h,uf} = \frac{\bar{h}_{h,uf} W}{k_n} = 0.664 Re_{h,uf}^{1/2} Pr_h^{1/3}$ where $Re_{h,uf} = \frac{V_h W}{\nu_h}$, valid for $\delta_{h,uf} < (H_{h,f} + s_1)/2$ (experimental module) or $\delta'_{h,uf} < \frac{H_{h,f}}{2}$ (actual heat exchanger)
Fluid flow in microchannels	Heat transfer coefficient: $\bar{Nu}_c = \frac{\bar{h}_c D_{c,eq}}{k_c} = 0.0214 \left[1.0 + \left(\frac{D_{c,eq}}{L}\right)^{2/3} \right] (Re_c^{0.8} - 100) Pr_c^{0.4}$ for $Pr_c < 1.5$, $Re_c > 10^4$ $\bar{Nu}_c = \frac{\bar{h}_c D_{c,eq}}{k_c} = 0.012 \left[1.0 + \left(\frac{D_{c,eq}}{L}\right)^{2/3} \right] (Re_c^{0.87} - 280) Pr_c^{0.4}$ for $Pr_c > 1.5$, $Re_c > 3000$ $\bar{Nu}_c = \frac{\bar{h}_c D_{c,eq}}{k_c} = \left\{ [2.22X^{-0.33}]^3 + Nu_{fd}^3 \right\}^{1/3}$ otherwise where $Re_c = \frac{V_c D_{c,eq}}{\nu_c}$, $D_{c,eq} = \frac{4(W_{c,cf} H_{c,cf})}{2(W_{c,cf} + H_{c,cf})}$, $X = \frac{L}{Pe D_{c,eq}}$, $Pe = Re_c Pr_c$, $Nu_{fd} = 8.235 [1 - 2.042\beta + 3.085\beta^2 - 2.477\beta^3 + 1.058\beta^4 - 0.186\beta^5]$, $\beta = \frac{W_{c,cf}}{H_{c,cf}}$
Airflow on back of module (Experimental module)	Heat transfer coefficient: $\bar{Nu}_{h,b} = \frac{\bar{h}_{h,b} D_{h,eq}}{k_n} = 1.86 \left(\frac{Re_{h,b} Pr_h}{W/D_{h,eq}} \right)^{1/3} \left(\frac{\mu_h}{\mu_{h,s}} \right)^{0.14}$ for $Pr_h < 5$ where $Re_{h,b} = \frac{V_h D_{h,eq}}{\nu_h}$, $D_{h,eq} = 2s_2$

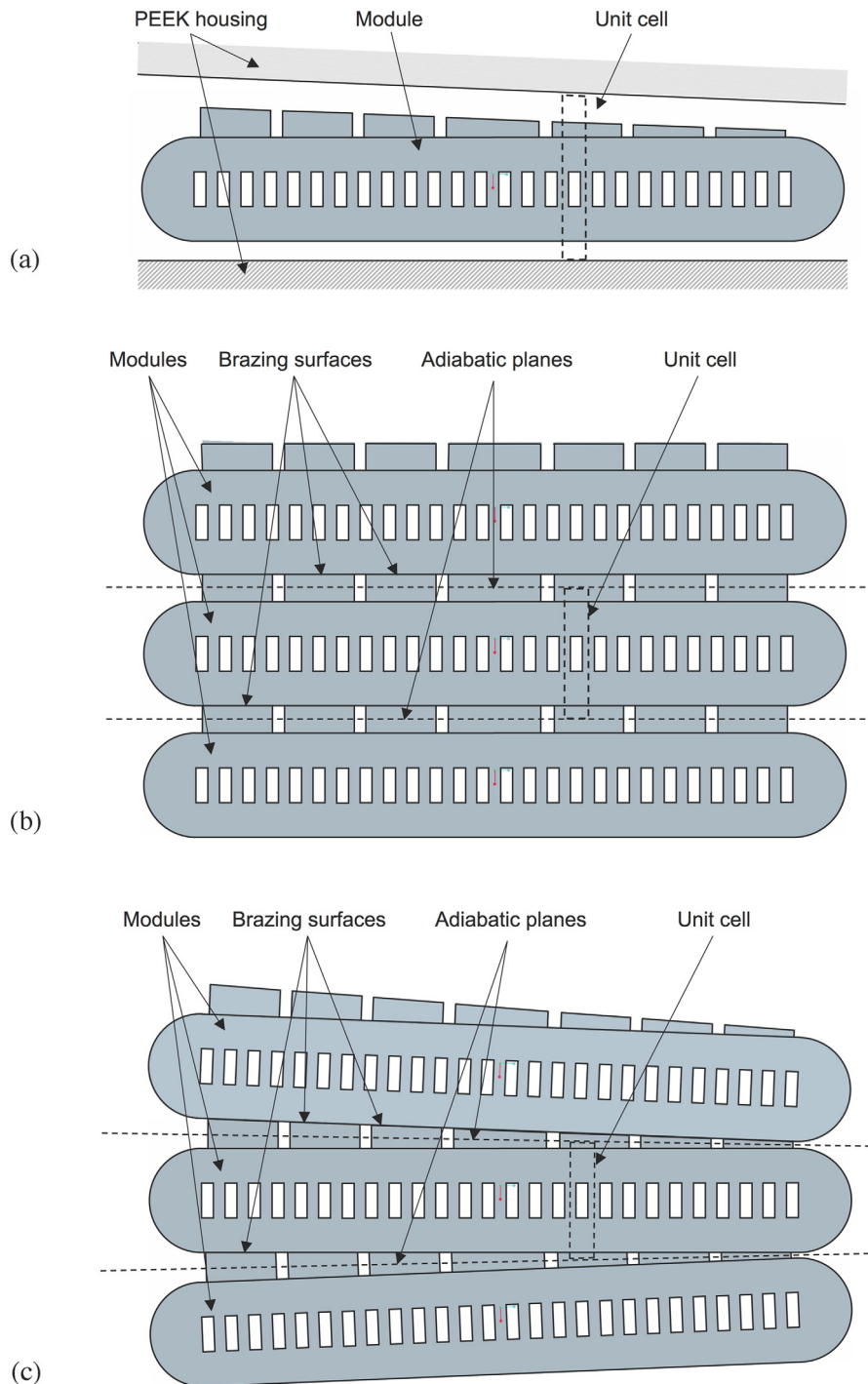


Fig. 5 Comparison of unit cell boundary conditions for: (a) experimental module, (b) module in rectangular heat exchanger, and (c) module in annular heat exchanger

These changes in boundary conditions will affect the airside portions of the resistance network as the boundaries of the cell are altered. While the general expression for $R_{h,1}$ from Eq. (3) remains changed—the heat is still transferred through the finned and unfinned portions of the surface—only half of the fin’s surface is participating, and the fin top is no longer available for convective heat transfer. Because of these changes, the equation for the airside finned area becomes

$$A'_{h,f} = N_{h,r} (W_{h,f} + L_{h,f}) H_{h,f} \quad (11)$$

The new, symmetrical nature of the heat transfer path means that the back surface of each module is now identical to the front sur-

face, which yields an airside resistance expression for surface 4 identical to that for surface 1.

$$R'_{h,4} = R'_{h,1} = \frac{1}{N_{h,f} [\eta'_{h,f} \bar{h}_{h,f} A'_{h,f} + \bar{h}_{h,uf} A_{h,uf}]} \quad (12)$$

A line of symmetry can also be drawn through the middle of the fuel microchannels. This drastically simplifies the analysis by allowing the microchannel sidewalls to be modeled as fins with adiabatic tips that are half the microchannel height. The rate of heat flow through the sidewalls becomes

$$q'_{c,sw} = N_{c,ch} \sqrt{\bar{h}_c P_{c,f} k_s A_{c,csf}} (T_2 - T_c) \tanh\left(m_c \frac{H_{c,ch}}{2}\right) \quad (13)$$

$$= \frac{(T_2 - T_c)}{\left\{ \frac{1}{N_{c,ch} \sqrt{\bar{h}_c P_{c,f} k_s A_{c,csf}} \tanh\left(m_c \frac{H_{c,ch}}{2}\right)} \right\}}$$

Because of symmetry, an equal heat flow rate is coming from surface 3 of the module. From Eq. (13), two equal resistances associated with heat flow through the symmetrical halves of the microchannel unit cell sidewalls can be expressed as

$$R'_{c,sw} = \frac{1}{N_{c,ch} \sqrt{\bar{h}_c P_{c,f} k_s A_{c,csf}} \tanh\left(\sqrt{\frac{\bar{h}_c P_{c,f} H_{c,ch}}{k_s A_{c,csf}}} \frac{H_{c,ch}}{2}\right)} \quad (14)$$

This means that the two parallel branches of the thermal resistance network in Fig. 4(a) can be simplified into one carrying half the module's heat rate as shown in Fig. 4(b).

These changes also affect the relations for airside heat transfer coefficient and fin efficiency. While the correlations used are the same, the boundary layer limitations are altered slightly. Also, since the model now assumes an airside fin with an adiabatic tip, the efficiency approximation is no longer needed. Table 1 summarizes the relations for the airside and fluid-side heat transfer coefficients and fins required for actual heat exchangers [13,17,18].

3.5 Validation of Model Predictions for Test Module. Because the correlations used in the analytical model were updated compared to those used by Nacke et al. [12], the code was again run against the experimental water data to validate the changes using the resistance network shown in Fig. 4(a). Figure 6 shows the percent error in predicting the air and water temperature drops across the module for three sets of operating conditions. As in the previous study, the percent temperature error is defined as

$$\% \text{Airside temperature error} = \frac{|T_{h,o,exp} - T_{h,o,th}|}{(T_{h,in,exp} - T_{h,o,exp})} \quad (15)$$

where $T_{h,in,exp}$, $T_{h,o,exp}$, and $T_{h,o,th}$ are the measured inlet temperature, measured mean outlet temperature, and predicted mean outlet temperature, respectively. Similarly, the percent temperature error for the waterside is defined as

$$\% \text{Waterside temperature error} = \frac{|T_{c,o,exp} - T_{c,o,th}|}{(T_{c,o,exp} - T_{c,in,exp})} \quad (16)$$

where $T_{c,in,exp}$, $T_{c,o,exp}$, and $T_{c,o,th}$ are the measured inlet temperature, measured mean outlet temperature, and predicted mean outlet temperature, respectively. Like the predictions of Nacke et al., the new error predictions for both streams are mostly below 15%, demonstrating that the changes to the code have not affected its accuracy.

4 Parametric Study and Overall Heat Exchanger Effectiveness

With the analytical model modified for use with actual heat exchangers, the module design can be optimized to maximize heat transfer rate. This can be accomplished with the aid of a parametric study in which a geometric parameter of the module is varied, while all other parameters are held constant. However, this method is complicated by the interdependence of several of the module's parameters on one another.

To reduce the overall number of variables in the optimization process, the overall length, L , and width, W , of the module are kept constant and equal to those of the experimental module,

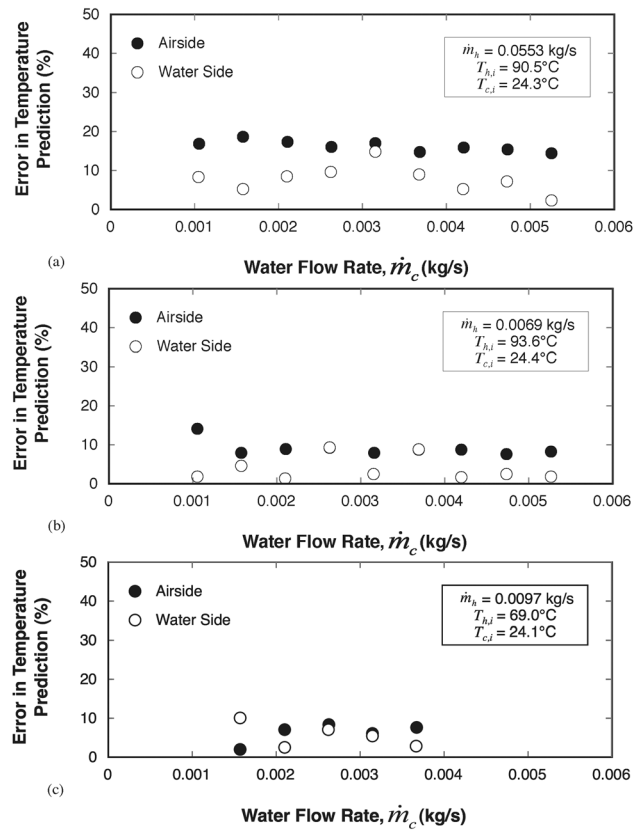


Fig. 6 Percent error in predicting airside and waterside temperature drop with water flow rate for: (a) $\dot{m}_h = 0.00553$ kg/s, $T_{h,i} = 90.5^\circ\text{C}$, and $T_{c,i} = 24.3^\circ\text{C}$, (b) $\dot{m}_h = 0.0069$ kg/s, $T_{h,i} = 93.6^\circ\text{C}$, and $T_{c,i} = 24.4^\circ\text{C}$, and (c) $\dot{m}_h = 0.0097$ kg/s, $T_{h,i} = 69.0^\circ\text{C}$, and $T_{c,i} = 24.1^\circ\text{C}$

66.04 and 15.24 mm, respectively. On the airside, fin height, $H_{h,f}$, fin width, $W_{h,f}$, fin length, $L_{h,f}$, width of channel between fin rows, $W_{h,ch}$, and number of fin rows, $N_{h,f}$, which are defined in Fig. 3(c), are all allowed to vary. Notice that $H_{h,f}$ can be altered without changing any of the other module parameters, but it will influence the overall thickness (outer envelope) of the module as discussed below. Notice that for a given value of $N_{h,f}$, $W_{h,f}$, and $W_{h,ch}$ are dependent on one another because L is constant. In the parametric analysis, when $W_{h,f}$ is varied, $W_{h,ch}$ is kept constant, and vice versa, by allowing $N_{h,f}$ to vary. Finally, because the overall module width, W , is kept constant, varying $L_{h,f}$ causes the number of fins in a single row, $N_{h,r}$, to vary as well. However, the overall length of all fins in a fin row is kept approximately constant.

On the fuel side, microchannel height, $H_{c,ch}$, microchannel width, $W_{c,ch}$, microchannel wall thickness, $W_{c,w}$, number of microchannels, $N_{c,ch}$, and the module's outer wall thickness, $H_{c,w}$, which are defined in Fig. 3(d), are all allowed to vary. Like the airside fin height, $H_{h,f}$, $H_{c,ch}$, and $H_{c,w}$ are independent of the other parameters and can be altered without changing any of the other parameters. For a given value of $N_{c,ch}$, $W_{c,ch}$, and $W_{c,w}$ are dependent on one another because W is constant. In the parametric analysis, when $W_{c,ch}$ is varied, $W_{c,w}$ is kept constant, and vice versa, by allowing $N_{c,ch}$ to vary.

The interdependence of several of the module's parameters makes it difficult to generate a broad range of values to examine. This is also complicated by the need to use whole numbers for $N_{h,f}$ and $N_{c,ch}$.

In an actual high-pressure-ratio turbine engine, the heat exchanger can encounter a range of temperatures, pressures, and flow rates from both the air and the fuel. Typical inlet operating ranges for air are flow rate of 0.45–1.81 kg/s, temperature of 504.6–560.2°C, and pressure of 1586.0–1724.0 kPa. For the fuel,

the inlet operating conditions are flow rate of 1.36–2.72 kg/s, temperature of 88.0–143.5 °C, and pressure of 8274.0–8550.0 kPa. Property values for air and JP-8 are obtained from Refs. [16] and [19], respectively. Initial heat exchanger module performance calculations showed small variations over the air and the fuel pressure and temperature ranges, evidenced by the relatively limited property variations. Therefore, specific temperatures and pressures were chosen, 560.2 °C and 1586 kPa for air, and 143.5 °C and 8274 kPa for JP-8, respectively.

The analytical model is applied for each set of module's geometrical parameters as well as for those of the experimental module using the resistance network shown in Fig. 4(b) to determine (a) the air outlet temperature for the assumed parameters, $T_{h,o,parameter}$, (b) the air outlet temperature based on the dimensions of the experimental module, $T_{h,o,module}$, (c) the fuel outlet temperature for the assumed parameters, $T_{c,o,parameter}$, and (d) the fuel outlet temperature based on the dimensions of the experimental module, $T_{c,o,module}$. A normalized temperature difference, defined as

$$\Delta T_{norm} = \frac{T_{h,in} - T_{h,out,parameter}}{T_{h,in} - T_{h,out,module}} = \frac{T_{c,out,parameter} - T_{c,in}}{T_{c,out,module} - T_{c,in}} \quad (17)$$

is used as a measure of the ability to enhance the module's effectiveness by changing the value of a given geometrical parameter. A ΔT_{norm} above unity amounts to an improvement in heat transfer performance compared to that of the experimental module.

Because of the previously stated interdependence of certain module parameters, the parametric study can be divided into three separate parts. The first encompasses those airside dimensions that are interdependent, the airside fin width, $W_{h,f}$, width of airside channel between fin rows, $W_{h,ch}$, and fin length, $L_{h,f}$. The second contains the interdependent fuel-side dimensions, the fuel microchannel width, $W_{c,ch}$, and microchannel wall thickness, $W_{c,w}$. The third includes the independent dimensions that will only affect the overall thickness of the module as they are varied, the airside fin height, $H_{h,f}$, the fuel microchannel height, $H_{c,ch}$, and the module's outer wall thickness, $W_{c,w}$. The values and ranges for each of these parameters that are considered in the optimization study are given in the third column of Table 2. Notice that the values for the number of airside fin rows, $N_{h,f}$, number of air fins in a single row, $N_{h,r}$, and number of microchannels, $N_{c,ch}$, are not included in the same column, because those values are not specified independently but rather allowed to vary with dimensions as discussed earlier.

Figures 7(a)–7(c) show the results of the first part of the optimization study, which concerns the interdependent airside param-

eters, $W_{h,f}$, $W_{h,ch}$, and $L_{h,f}$. Smaller values of all three parameters appear to increase the normalized temperature difference, yielding a heat transfer performance superior to that of the experimental module. The effect of the latter parameter is most obvious, since shorter airside fins reduce the overall thickness of the airside boundary layer.

Figures 7(d) and 7(e) show the results of the second part of the optimization study, namely, those related to the interdependent fuel-side parameters, $W_{c,ch}$ and $W_{c,w}$. Figure 7(d) shows better performance can be realized by decreasing microchannel width. The opposite is true for the microchannel wall thickness; Fig. 7(e) shows that increasing $W_{c,w}$ results in the larger normalized temperature difference.

The third part of the optimization study involves independent parameters, whose dimensions are not constrained by the constant width and length of the module but will influence the overall thickness of the module. The module thickness is an important factor in the design of the final heat exchanger. Increasing or decreasing the module thickness will cause a respective increase or decrease in the heat exchanger volume. In the same way, if it is desired to keep the volume of the heat exchanger constant, any increase or decrease in the module thickness will have to be counteracted by decreasing or increasing the number of modules in the heat exchanger.

Figures 8(a)–8(c) show the results from the third part of the optimization study. As to be expected, increasing the air fin height, $H_{h,f}$, increases the normalized temperature difference. On the other hand, increasing the fuel microchannel height, $H_{c,ch}$, or the module's outer wall thickness, $W_{c,w}$, has an adverse effect on temperature difference. The effect of the latter can be easily explained by the increased thermal resistance across the outer wall of the module.

The values of the various geometrical parameters determined from the optimization study are listed in the fourth column of Table 2. However, these theoretical optimum values must be tempered by practical manufacturing limitations as well as the operating environment of high-pressure-ratio turbine engines. For example, the optimum airside fin length of $L_{h,f} = 0.254$ mm (0.010 in.) is deemed far too small to fabricate and/or too fragile, and after consulting with microfabrication specialists, had to be doubled in size. Also, while the optimization study calls for minimizing the airside channel width, $W_{h,ch}$, fuel microchannel width, $W_{c,ch}$, and fuel microheight, $H_{c,ch}$, these three parameters are constrained by a practical minimum value of about 0.762 mm (0.03 in.) to prevent the fuel passages from being clogged by fuel coking of debris, or air passages by dust particles, especially in a desert

Table 2 Results of parametric study

Airsides geometry, mm (in.)				
Parameter	Experimental module dimensions	Values considered in optimization	Optimized values	Values recommended for heat exchanger
$H_{h,f}$ (Average value)	0.381 (0.015)	0.254–2.54 (0.010–0.100)	2.54 (0.100)	1.016 (0.040)
$W_{h,f}$	0.508 (0.020)	0.127, 0.762 (0.005, 0.030)	0.127 (0.005)	0.254 (0.010)
$L_{h,f}$ (Average value)	1.598 (0.0629)	0.254–1.778 (0.010–0.070)	0.254 (0.010)	0.508 (0.020)
$W_{h,ch}$	0.508 (0.020)	0.127, 0.762 (0.005, 0.030)	0.127 (0.005)	0.762 (0.030)
$N_{h,f}$	65	N/A	N/A	65
$N_{h,r}$	7	N/A	N/A	22
Fuel side geometry, mm (in.)				
Parameter	Experimental module dimensions	Values considered in optimization	Optimized values	Values recommended for heat exchanger
$W_{c,ch}$	0.254 (0.010)	0.0762, 0.406 (0.003, 0.016)	0.0762 (0.003)	0.762 (0.030)
$H_{c,ch}$	0.762 (0.030)	0.254–1.524 (0.010–0.060)	0.254 (0.010)	0.762 (0.030)
$W_{c,w}$	0.254 (0.010)	0.0762, 0.406 (0.003, 0.016)	0.406 (0.016)	0.889 (0.035)
$H_{c,w}$	0.762 (0.030)	0.254–1.524 (0.010–0.060)	0.254 (0.010)	0.254 (0.010)
$N_{c,ch}$	26	N/A	N/A	8

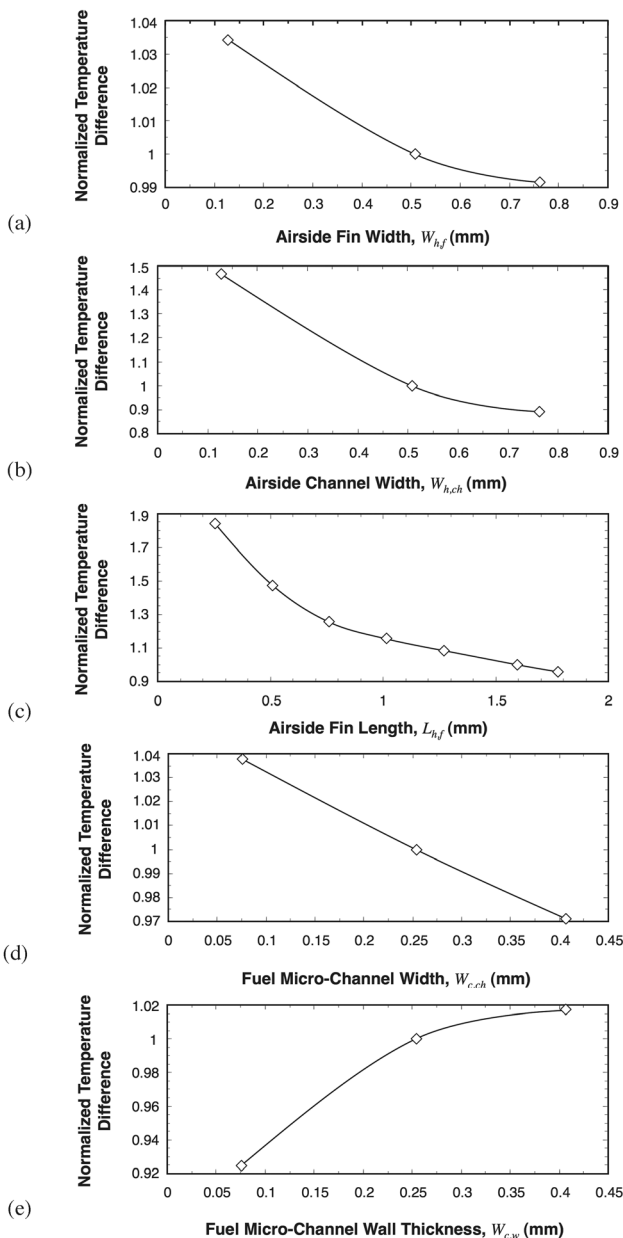


Fig. 7 Variation of normalized temperature difference with: (a) airside fin width, (b) airside channel width, (c) airside fin length, (d) fuel microchannel width, and (e) fuel microchannel wall thickness

environment. These constraints prevented the chosen microchannel wall thickness of $W_{c,w} = 0.406$ (0.016 in.) and airside fin width $W_{h,f} = 0.127$ mm (0.005 in.) from yielding whole number of microchannels, $N_{c,ch}$, and airside fin rows, $N_{h,f}$. To solve this problem, ΔT_{norm} was recalculated with the new values for $W_{h,ch}$, $W_{c,ch}$, and $H_{c,ch}$. Figure 8(d) shows the results for the airside, where the number of airside fin rows, $N_{h,f}$, is varied, which in turn varies the airside fin width, $W_{h,f}$. The dimensionless temperature change stays mostly constant, dropping off around 80 airside channels. Therefore, the specific number of channels is less important, and a value is chosen that yields a whole number of airside fin rows, and an airside fin width of $W_{h,f} = 0.254$ mm (0.010 in.) that is easily machinable. The same process is used for the fuel side; the number of microchannels, $N_{c,ch}$, is varied, which in turn varies the microchannel wall thickness, $W_{c,w}$. Figure 8(e) shows that the dimensionless temperature difference is above unity for values less than 10. Therefore, using the same requirements as the air-

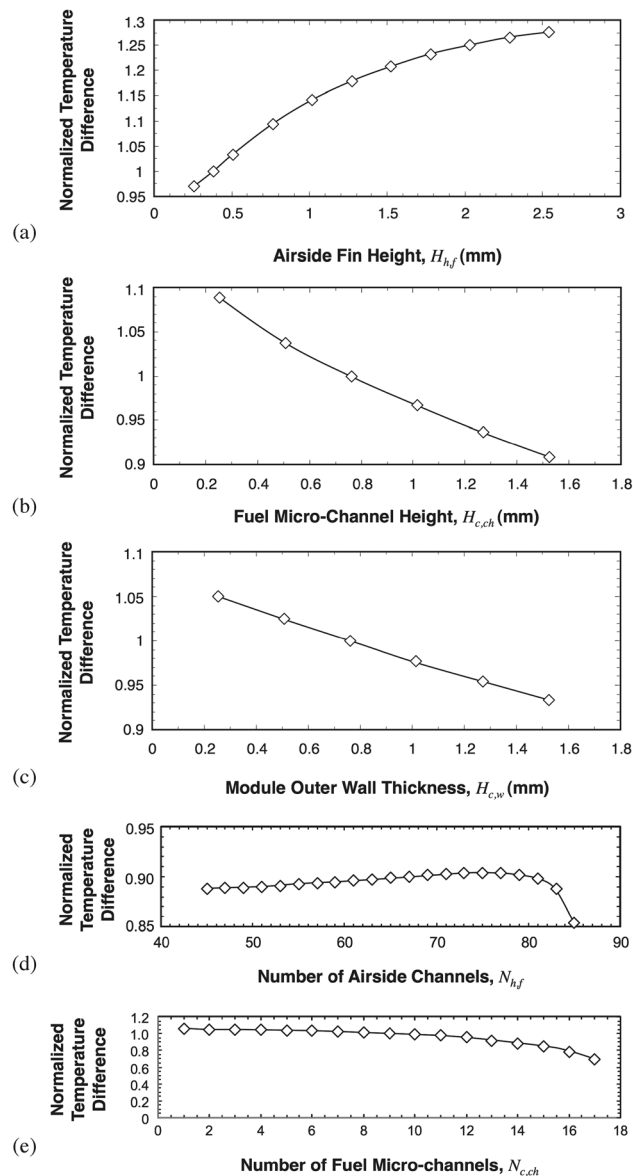


Fig. 8 Variation of normalized temperature difference with: (a) airside fin height, (b) fuel microchannel height, (c) module's outer wall thickness, (d) number of airside fins rows for constant airside channel width, and (e) number of fuel microchannels for constant microchannel width

side—a whole number of microchannels and an airside fin width that is easily machinable—eight microchannels are chosen, which correspond to a microchannel wall thickness of $W_{c,w} = 0.406$ (0.016 in.). Finally, the optimization study also showed that increasing the air fin height, $H_{h,f}$, should yield a monotonic increase in the normalized temperature difference. However, increasing $H_{h,f}$ also increases the module thickness and, in turn, the volume of the final heat exchanger. The value of $H_{h,f} = 1.016$ mm (0.040) was ultimately chosen based on this consideration and the aforementioned need to avoid clogging of the air passages.

Taking all these practical consideration and limitations into account, the optimized values were modified to arrive at more realistic dimensions that are more compatible with high-pressure-ratio turbine engines. These dimensions are listed in the final column of Table 2.

Once the realistic module geometry is decided upon, a full heat exchanger can be modeled and analyzed. Two different design

configurations are examined here, the rectangular, Fig. 1(b), and the annular, Fig. 1(c).

The most widely used technique for assessing heat exchanger performance is effectiveness, or the ratio of the heat exchanger's actual to maximum possible heat transfer rate.

$$\varepsilon = \frac{\dot{m}_h \text{HEXC}_{p,h} (T_{h,in} - T_{h,out})}{\dot{m}_{\min, \text{HEXC}_{p,\min}} (T_{h,in} - T_{c,in})} = \frac{\dot{m}_c \text{HEXC}_{p,c} (T_{c,out} - T_{c,in})}{\dot{m}_{\min, \text{HEXC}_{p,\min}} (T_{h,in} - T_{c,in})} \quad (18)$$

where $\dot{m}_{\min, \text{HEXC}_{p,\min}}$ is the smaller of $\dot{m}_h \text{HEXC}_{p,h}$ or $\dot{m}_c \text{HEXC}_{p,c}$ [13]. Other parameters, such as the NTU, must be used in complicated heat exchanger effectiveness relations, because the temperatures are not known in advance. However, the present analytical model alleviates this problem and allows the direct use of Eq. (18).

Figure 9(a) shows effectiveness results versus fuel flow rate for the rectangular heat exchanger with one air pass and one, two, and three fuel passes as illustrated in Fig. 1(b). For each design, effectiveness values are presented for two heat exchanger designs, the first containing 64 modules per fuel pass, and the second 92 modules. For all cases, the effectiveness increases with increasing fuel flow rate, anywhere from 6% to 12%. Adding passes also increases the effectiveness, especially for the larger design containing 92 modules per pass because of the added surface area. On average, the larger design yields effectiveness values of 0.329 versus 0.275 for the smaller design for the one fuel-pass design, and 0.626 versus 0.566 for the three fuel-pass design.

Figure 9(b) shows the effectiveness results for the annular heat exchanger with one air pass and one, two, and three fuel passes. Here also, two designs are considered, which both contain 267 modules in the outer fuel pass and 52 modules in the inner. However, the middle fuel pass contains 107 fuel modules in the first design and 178 modules in the second design. The number of modules is varied in the middle pass instead of the inner or outer passes in order to preserve the inner and outer diameters of the heat exchanger, which are important when placing an annular heat exchanger in an actual turbine engine. Figure 9(b) shows that, in all cases, the effectiveness increases with increasing fuel flow rate, especially with more fuel passes. The effectiveness is the same for the first pass of each design, because their outer passes

are identical. However, for the second pass, the design with the larger middle segment has the higher effectiveness—an average of 0.662 versus 0.634. This enhancement carries on to the third pass; even though the inner passes of each design are the same, the second design has the larger three-pass effectiveness.

For the most effective rectangular and annular designs, the mass flow rates, specific heats, and temperature changes for the air and the fuel were used to find the amount of heat rejected by the air and absorbed by the fuel. These values were then averaged to find the amount of heat transferred in each pass. For the rectangular design, 201.19, 113.61, and 65.68 kW of heat were transferred in the first, second, and third passes, respectively. For the annular design, 316.76, 88.37, and 22.76 kW of heat were transferred in the outer, middle, and inner passes, respectively. The large differences in heat transfer rate among the different passes in the annular design are mostly the result of differences in the number of modules per pass.

With the average volume of one module calculated at approximately 2.301 cm^3 , the heat transfer rate per unit volume for the first, second, and third passes of the rectangular design are 950.52, 536.73, and 310.31 W/cm^3 , respectively. Values for the annular design are 515.66, 215.79, and 190.25 W/cm^3 for the outer, middle, and inner passes, respectively.

5 Conclusions

This study examined the design of highly compact air–fuel heat exchangers for high-pressure-ratio aircraft turbine engines. The basic building block of this design is a miniature module that features parallel microchannels that serve as fuel flow passages, while the air flows externally perpendicular to the direction of the fuel flow over rows of short, straight fins. A large number of these modules are brazed together to form a turbine engine heat exchanger. Key findings from the study are as follows:

- (1) A theoretical model recently developed by the authors for a single module was validated experimentally by simulating aircraft fuel with water. For most tests, outlet temperatures for both air and liquid are predicted with an error of less than 15%. This error can be attributed to: (a) limitations of the one-dimensional assumptions used to calculate the overall heat transfer coefficient, (b) minor heat loss from the test module, and (c) experimental uncertainty of the measurement instruments used.
- (2) The model was expanded to actual heat exchangers and JP-8 aircraft fuel. On the airside of the module, superior performance is achieved by decreasing fin length, which yields an overall thinning of the air boundary layers with boundary layer re-initiation, decreasing the gap width between fins, which decreases the hydraulic diameter, and by decreasing fin width. On the fuel side, heat transfer performance is enhanced by decreasing the width of the fuel microchannels, which decreases the hydraulic diameter, and increasing the thickness of the walls separating microchannels, which increases the fin effectiveness of the walls.
- (3) The optimum dimensions of the module were adjusted based on several practical considerations. For example, manufacturing concerns resulted in thicker air fins than recommended by the model. The fuel microchannel's width had to be increased from the ideal value to avoid clogging of fuel passages by fuel coking or debris. Similarly, the gap between air fins had to be increased from the optimum value to preclude clogging.
- (4) This study showed the versatility of the module design in adapting to different heat exchanger geometries and design envelopes as demanded by the turbine engine. It is shown that modules can be brazed together into both rectangular and radial configurations, and design concepts are presented for each configuration using a single air pass and one, two, or three fuel passes.

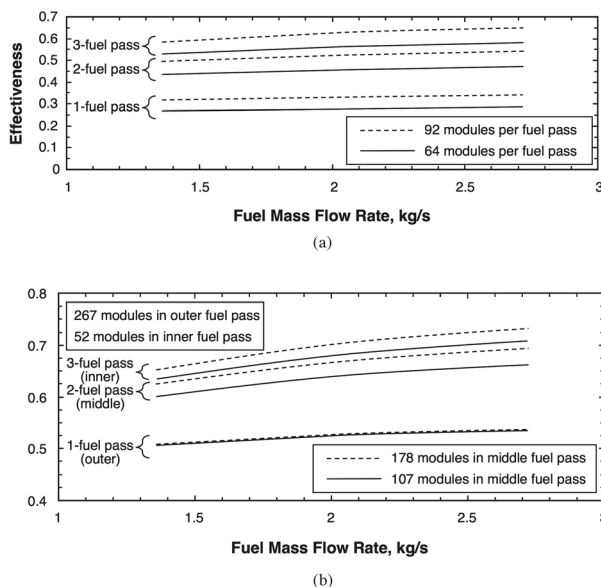


Fig. 9 Effectiveness results for: (a) rectangular heat exchanger with one air pass and one, two, and three fuel passes and (b) annular heat exchanger with one air pass and one, two, and three fuel passes

(5) The model is highly effective at generating heat exchanger effectiveness predictions for both the rectangular and the annular configurations. For each configuration, higher effectiveness is achieved by increasing the number of fuel passes and/or increasing the fuel flow rate.

The authors are presently pursuing methods to predict pressure drop across the air and the fuel sides, which, aside from the heat transfer analysis provided in this study, are important to the overall assessment of heat exchanger performance.

Acknowledgment

The authors are grateful for the financial support of Rolls-Royce and LibertyWorks through the Rolls-Royce Purdue University Technology Center (UTC).

Nomenclature

a = airside parameter defined in Eq. (5a)
 $A_{c,csf}$ = fuel (or water) fin cross-sectional area
 $A_{h,csf}$ = air fin cross-sectional area
 $A_{h,f}$ = airside finned area
 $A'_{h,f}$ = airside finned area for actual heat exchanger module
 $A_{h,uf}$ = airside unfinned area
 b = fuel-side (or waterside) parameter defined in Eq. (5b)
 c_p = specific heat at constant pressure
 $D_{c,eq}$ = fuel-side (or waterside) microchannel hydraulic diameter
 $D_{h,eq}$ = airside hydraulic diameter on back of module
 $H_{c,ch}$ = fuel-side (or waterside) microchannel height
 $H_{c,w}$ = module's outer wall thickness
 $H_{h,f}$ = airside fin height
 $H_{h,fe}$ = corrected airside fin height
 \bar{h}_c = average fuel-side (or waterside) heat transfer coefficient
 $\bar{h}_{h,b}$ = average airside heat transfer coefficient on back of module
 $\bar{h}_{h,f}$ = average airside fin heat transfer coefficient
 $\bar{h}_{h,uf}$ = average airside heat transfer coefficient along surface between fins
 k_c = thermal conductivity of fuel (or water)
 k_h = thermal conductivity of air
 k_s = thermal conductivity of heat exchanger module
 L = length of module in direction of fuel (or water) flow
 $L_{h,f}$ = airside fin length
 m_c = fuel-side (or waterside) fin parameter
 m_h = airside fin parameter
 \dot{m}_c = fuel (or water) mass flow rate
 \dot{m}_h = air mass flow rate
 $N_{c,ch}$ = number of fuel-side (or waterside) microchannels
 $N_{h,f}$ = number of airside fin rows
 $N_{h,r}$ = number of small fins in airside fin row
 \bar{Nu}_c = average fuel-side (or waterside) Nusselt number
 $\bar{Nu}_{h,b}$ = average airside Nusselt number on back of module
 $\bar{Nu}_{h,f}$ = average airside Nusselt number on finned side of module along fins
 $\bar{Nu}_{h,uf}$ = average airside Nusselt number on finned side of module between fins
 $P_{c,f}$ = fuel (or water) fin perimeter
 $P_{h,f}$ = air fin perimeter
 Pr = Prandtl number
 q = heat exchanger module's heat transfer rate
 q'' = heat flux across module
 $q_{a,b}$ = back surface heat transfer rate
 $q_{c,exp}$ = measured waterside heat transfer rate
 $q_{c,th}$ = theoretical waterside heat transfer rate
 $q_{c,sw}$ = fuel-side (or waterside) microchannel sidewall heat transfer rate

$q'_{c,sw}$ = fuel-side (or waterside) microchannel sidewall heat transfer rate for actual heat exchanger module
 $q_{c,2}$ = surface 2 convective heat transfer rate
 $q_{c,3}$ = surface 3 convective heat transfer rate
 $q_{h,exp}$ = measured airside heat transfer rate
 $q_{h,th}$ = theoretical airside heat transfer rate
 $q_{h,1}$ = surface 1 heat transfer rate
 q_s'' = heat flux across module's outer wall
 R_A = thermal resistance of branch A of module's equivalent resistance
 R_B = thermal resistance of branch B of module's equivalent resistance
 $R_{c,2}$ = surface 2 base convective resistance
 $R_{c,3}$ = surface 3 base convective resistance
 R_{cond} = module's outer wall conduction resistance
 $R_{c,sw1}$ = first fuel (or water) sidewall resistance
 $R_{c,sw2}$ = second fuel (or water) sidewall resistance
 $R'_{c,sw2}$ = fuel (or water) sidewall resistance for actual heat exchanger module
 $R_{h,1}$ = airside resistance
 $R'_{h,1}$ = airside resistance for actual heat exchanger module
 $R_{h,4}$ = airside base resistance
 $R'_{h,4}$ = airside base resistance for actual heat exchanger module
 R_{tot} = total (equivalent) resistance
 Re_c = fuel-side (or waterside) Reynolds number
 $Re_{h,b}$ = airside Reynolds number on back of module
 $Re_{h,f}$ = airside Reynolds number on finned side of module along fins
 $Re_{h,uf}$ = airside Reynolds number on finned side of module between fins
 s_1 = flow clearance above airside fin tip
 s_2 = flow clearance along back of module
 T = temperature
 T_1 = surface 1 temperature
 T_2 = surface 2 temperature
 T_3 = surface 3 temperature
 T_4 = surface 4 temperature
 T_c = fuel (or water) temperature
 $T_{c,in,exp}$ = measured waterside inlet temperature
 $T_{c,o}$ = mean outlet fuel (or water) temperature
 $T_{c,o,exp}$ = measured waterside mean outlet temperature
 $T_{c,o,th}$ = theoretical waterside outlet temperature
 T_h = air temperature
 $T_{h,in,exp}$ = measured airside inlet temperature
 $\bar{T}_{h,o}$ = mean outlet air temperature
 $T_{h,o,exp}$ = measured airside mean outlet temperature
 $T_{h,o,th}$ = theoretical airside mean outlet temperature
 U = overall heat transfer coefficient
 V_c = fuel-side (or waterside) mean velocity
 V_h = airside mean velocity
 W = width of module in direction of air flow
 $W_{c,ch}$ = fuel-side (or waterside) microchannel width
 $W_{c,w}$ = fuel-side (or waterside) microchannel wall thickness
 $W_{h,ch}$ = airside channel width
 $W_{h,f}$ = airside fin width
 x = fuel (or water) direction coordinate
 x' = dimensionless fuel (or water) direction coordinate
 y = air direction coordinate
 y' = dimensionless air direction coordinate

Greek Symbols

$\delta_{h,f}$ = airside finned boundary layer thickness
 $\delta_{h,uf}$ = airside unfinned boundary layer thickness
 $\eta_{h,f}$ = airside fin efficiency
 $\eta'_{h,f}$ = airside fin efficiency for actual heat exchanger module
 θ = local dimensionless temperature difference between air and fuel (or water)
 μ = dynamic viscosity

ν = kinematic viscosity
 ϕ = ratio of mean to initial temperature difference

Subscripts

c = cold fuel stream (or simulated water stream)
 h = hot air stream
HEX = heat exchanger
module = based on dimensions of experimental module
norm = normalized
 s = solid surface

References

- [1] Rolls-Royce, 1996, *The Jet Engine*, 5th ed., Rolls-Royce plc, Derby, England.
- [2] Bruening, G. B., and Chang, W. S., 1999, "Cooled Cooling Air Systems for Turbine Thermal Management," ASME Paper No. 99-GT-14.
- [3] Huang, H., Spadaccini, L. J., and Sobel, D. R., 2004, "Fuel-Cooled Thermal Management for Advanced Aero Engines," *ASME J. Eng. Gas Turbines Power*, **126**, pp. 284–293.
- [4] Kibbey, T. P., 2004, "Impinging Jets for Application in High-Mach Aircraft Thermal Management," M.S. thesis, Purdue University, West Lafayette, IN.
- [5] Herring, N. R., and Heister, S. D., 2009, "On the Use of Wire Coil Inserts to Augment Tube Heat Transfer," *J. Enhanced Heat Transfer*, **16**, pp. 19–34.
- [6] Willingham, T. C., and Mudawar, I., 1992, "Channel Height Effects on Forced-Convection Boiling and Critical Heat Flux From a Linear Array of Discrete Heat Sources," *Int. J. Heat Mass Transfer*, **35**, pp. 1865–1880.
- [7] Mudawar, I., 2001, "Assessment of High-Heat-Flux Thermal Management Schemes," *IEEE Trans. Compon. Packag. Technol.*, **24**, pp. 122–141.
- [8] Mudawar, I., and Wadsworth, D. C., 1991, "Critical Heat Flux From a Simulated Electronic Chip to a Confined Rectangular Impinging Jet of Dielectric Liquid," *Int. J. Heat Mass Transfer*, **34**, pp. 1465–1480.
- [9] Wadsworth, D. C., and Mudawar, I., 1992, "Enhancement of Single-Phase Heat Transfer and Critical Heat Flux From an Ultra-High-Flux Simulated Microelectronic Heat Source to a Rectangular Impinging Jet of Dielectric Liquid," *ASME J. Heat Transfer*, **114**, pp. 764–768.
- [10] Rybicki, J. R., and Mudawar, I., 2006, "Single-Phase and Two-Phase Cooling Characteristics of Upward-Facing and Downward-Facing Sprays," *Int. J. Heat Mass Transfer*, **49**, pp. 5–16.
- [11] Ujereh, S., Fisher, T., and Mudawar, I., 2007, "Effects of Carbon Nanotube Arrays on Nucleate Pool Boiling," *Int. J. Heat Mass Transfer*, **50**, pp. 4023–4038.
- [12] Nacke, R., Northcutt, B., and Mudawar, I., 2011, "Theory and Experimental Validation of Cross-Flow Micro-Channel Heat Exchanger Module With Reference to High Mach Aircraft Gas Turbine Engines," *Int. J. Heat Mass Transfer*, **54**, pp. 1224–1235.
- [13] Incropera, F., Dewitt, D., Bergman, T., and Lavine, A., 2007, *Fundamentals of Heat and Mass Transfer*, 6th ed., Wiley, Hoboken, NJ.
- [14] Mason, J. L., 1954, "Heat Transfer in Crossflow," Proceedings of the 2nd U.S. National Congress of Applied Mechanics, Ann Arbor, MI, pp. 801–803.
- [15] Beyer, W. H., 1976, *Standard Mathematical Tables*, 24th ed., CRC Press, Cleveland, OH.
- [16] Klein, S. A., 2011, *Engineering Equation Solver (EES)*, F-Chart Software, Madison, WI.
- [17] Gnielinski, V., 1976, "New Equations for Heat and Mass Transfer in Turbulent Pipe and Channel Flow," *Int. Chem. Eng.*, **16**, pp. 359–368.
- [18] Copeland, D., Behnia, M., and Nakayama, W., 1996, "Manifold Microchannel Heat Sinks: Isothermal Analysis," Proceedings of the 5th Intersociety Conference on Thermal Management in Electronic Systems (I-THERM V), Orlando, FL, pp. 251–257.
- [19] Huber, M. L., 2003, NIST Thermophysical Properties of Hydrocarbon Mixtures Database (SUPERTRAPP), NIST Standard Reference Database 4, National Institute of Standards and Technology, Gaithersburg, MD.